Food & Function

ROYAL SOCIETY OF CHEMISTRY

PAPER

View Article Online
View Journal | View Issue

Cite this: *Food Funct.*, 2025, **16**, 2124

Development of 3D-printed foods incorporating riboflavin-loaded whey protein isolate nanostructures: characterization and *in vitro* digestion†

João F. Araújo, [a] Jean-Michel Fernandes, [a] Daniel Madalena, [a] Raquel F. S. Gonçalves,[a] Jorge M. Vieira,[a,b] Joana T. Martins, [a,b] António A. Vicente [a,b] and Ana C. Pinheiro *[a,b]

3D printing has emerged as a groundbreaking technology, aiming to enhance sensory attributes and improving nutritional/functional aspects. Simultaneously, nano-delivery systems have emerged as an opportunity to protect bioactive compounds against degradation and improve their bioaccessibility. Therefore, a novel concept is underway, involving the 3D printing of perishable healthy foods previously fortified with bioactive compound-loaded nanostructures. As a model concept, whey protein isolate (WPI) nanostructures were associated with riboflavin with an efficiency of 59.2%. Carrot pastes with adequate printability, shape retention and rheological characteristics were formulated. Riboflavin-WPI loaded nanostructures were incorporated into carrot inks and submitted to a static *in vitro* digestion. There was a notable increase in riboflavin bioaccessibility (+23.1%), suggesting a synergistic interaction between WPI nanostructures and carrot matrix. These results may contribute to validating the use of WPI nanostructures as effective encapsulating systems allied with 3D food printing towards the development of functional foods with personalized structure and nutrition profile.

Received 18th October 2024,
Accepted 12th February 2025

DOI: 10.1039/d4fo05102e

rsc.li/food-function

1. Introduction

The scientific evidence supporting a correlation between dietary elements and prevalent diseases like heart disease, stroke, type 2 diabetes, and cancer has spurred the exploration for functional foods and the use of innovative technologies. Researchers are delving into alternatives to address consumer needs through the creation of functional foods tailored to personalized nutritional profiles. Advancements in food science and technology present solutions, particularly for specific populations with distinct nutritional requirements, such as the elderly (*e.g.*, prone to dysphagia) and children (*i.e.*, requiring increased fruit/vegetable intake). Despite the scientific progress, concerns regarding the sustainability and marketability of functional foods with specific functionalities or personalized nutrition have surfaced due to production costs and consumer acceptance.[1,2] In the sense of a healthy and diversified diet, the consumption of fruits and vegetables is of utmost importance for the general population. When considering the diet of the elderly, the organoleptic properties of such foods (*e.g.*, appearance, flavor and mouthfeel) are crucial for their acceptability and regular consumption. Additionally, due to the limited capacity of the elderly to consume foods of any kind, their nutrition can be significantly affected given the low intake of daily required macro- and micro-nutrients (*e.g.*, proteins, fibers, vitamins and minerals).[3–6]

Over recent years, 3D food printing (3DFP) has garnered significant attention, prompting relevant studies aimed at developing 3D-printed foods (3DPF) endowed with distinctive organoleptic and functional features, tailored functional properties for niche markets, and personalized nutritional profiles.[7–9] This technology offers a dual benefit in food manufacturing by enhancing the sensorial attributes and nutritional/functional content of functional foods.[10,11] 3DFP allows users to exert control over various printing parameters, including the quantity and type of printing ingredients, optimizing the food structure to align with consumption preferences. Notably, it facilitates the reduction of food waste by printing only the required amount and utilizing perishable fruits, vegetables, or by-products to craft appealing foods.[12–15] This ability to improve sensorial and nutritional aspects of vegetables and fruits is aligned with the criteria of the consumer's choice to purchase

[a]*CEB – Centre of Biological Engineering, University of Minho, Portugal.*
E-mail: anapinheiro@ceb.uminho.pt
[b]*LABBELS – Associate Laboratory, Braga, Guimarães, Portugal*

† Electronic supplementary information (ESI) available. See DOI: https://doi.org/10.1039/d4fo05102e

food (*i.e.*, appearance, taste, cost, experience, convenience and nutrition) as mentioned by Ringquist *et al.* (2016).[16] Rheological attributes stand as pivotal physicochemical parameters, significantly impacting the printability of a food ink. Among several others, hydrocolloids such as xanthan gum (XG) play a pivotal role in altering the rheological properties and textures of materials.[8,17]

In this study, carrot was selected as a model perishable food based on two main criteria: (1) due to its valuable nutritional profile (*i.e.*, source of beta-carotene, fibers, vitamin K1, potassium, antioxidants, among others), interesting composition in macronutrients (*i.e.*, carbohydrates); and (2) due to its high water composition (>80%) that makes this healthy vegetable a good candidate for nanostructure dispersion and further formulation for 3DFP.

The innovative approach of fortifying foods with nanostructures encapsulating bioactive compounds aims at developing specifically tailored foods with high protection of the bioactive compounds against environmental factors such as light, pH and temperature, and digestion. Whey protein isolate (WPI) is a promising candidate for devising delivery systems ensuring the controlled release of bioactive compounds.[18]

In line with this, the convergence of two emerging technologies, 3DFP and nanotechnology, opens opportunities for developing personalized, cartridge-based food formulations with enhanced bioactive compound bioavailability, offering an improved consumption experience and nutrition. However, despite their potential, the utilization of nano-size particles raises concerns about altering their biological fate, potentially posing risks to human health. In compliance with EU regulations, any nano-derived food ingredient must undergo a thorough safety assessment before approval for use.[19] A crucial aspect involves comprehending the behavior of nanostructures during digestion/absorption, evaluating their efficiency and safety, facilitating their widespread integration into the realm of food applications. Additionally, considering the influence of the food matrix on the gastrointestinal fate of nanostructures/bioactive compounds, safety assessments should follow the incorporation of nanostructures into food inks.

In this work, WPI nanostructures were prepared through the thermal gelation method, to associate Rb as hydrophilic model compound. WPI nanostructures were then incorporated in carrot inks, prepared with increasing concentrations of XG which were previously characterized in terms of their rheological behavior, aiming at the selection of the ideal carrot ink formulation for further applications. Cell viability studies and an *in vitro* digestion adapted to the general older adult population were then performed to determine WPI-Rb nanostructures' safety and Rb bioaccessibility before and after incorporation in the food inks. The use of WPI to produce nanostructures has been extensively studied as reported elsewhere.[18,20–23]

This research introduces an emerging innovation through the combination of nano delivery systems and 3D food printing, aiming at the development of functional foods with customizable nutritional and rheological profiles. Also, it provides valuable insights into food ink rheological characteristics, offering an understanding of influence of the physical and mechanical aspects of studied inks and finally, the impact on 3DPFs' shape printability. Furthermore, the positive impact of the encapsulation of WPI nanostructures and their incorporation into the food matrix on Rb bioaccessibility was also validated.

2. Materials and methods

2.1. Chemicals and materials

Rb (≥98%), XG (*Xanthomonas campestris*), penicillin/streptomycin solution (contains 10 000 units penicillin and 10 mg streptomycin per mL) (PS), trypsin-EDTA, and MTT (3-(4,5–126 dimethylthiazol-2-yl)-2,5-diphenyltetrazolium bromide) and sodium phosphate tribasic dodecahydrate 98% were purchased from Sigma-Aldrich (St Louis, MO, USA). WPI powder (Lacprodan DI-9212) was kindly supplied by Arla (Arla Foods, Viby, Denmark). In accordance with information provided by the supplier, WPI powder was essentially free of fat (max. 0.2%) and lactose (max. 0.5%). Protein composition, determined by reversed-phase high-performance liquid chromatography (RH-HPLC) as described elsewhere,[24] was as follows: α-lactalbumin (α-lac) 22.8%, bovine serum albumin (BSA) 1.7%, β-lgA 44%, β-lgB 30.7%, and immunoglobulins (IG) 1.1%, on a protein basis. Hydrochloric acid and monosodium phosphate were purchased from Panreac (Barcelona, Spain), and sodium phosphate dibasic was obtained from Chem-Lab (Zedelgem, Belgium). Dimethyl sulfoxide (≥99.0%) (DMSO) was purchased from Fisher Scientific (NJ, USA). All chemicals used were of analytical grade. Dulbecco's modified Eagle's medium (DMEM), non-essential amino acids (NEAA) and phosphate-buffered saline (PBS) were obtained from Lonza (Basel, Switzerland). Heat-inactivated fetal bovine serum (FBS) was obtained from Merck (Darmstadt, Germany). Human colon Caco-2 cell line (American Type Culture Collection, ATCC) was kindly provided by the Department of Biology of the University of Minho (Braga, Portugal). Carrots were purchased in a local supermarket (Braga, Portugal), refrigerated at 4 °C for a maximum of two days until used.

2.2. Production of WPI-Rb nanostructures

2.2.1. Preparation. WPI nanostructures were prepared following the optimized protocol outlined by Simões *et al.* (2020) with some modifications.[25] In this process, WPI powder was utilized to produce nanostructures (0.5%), in 10 mmol L^{-1} sodium phosphate buffer at pH 7. The pH was adjusted to 6 using 0.5 mol L^{-1} H_3PO_4, as needed. The solutions underwent continuous stirring for 2 h at 400 rpm at room temperature. To ensure complete protein rehydration, the WPI dispersions were left overnight at 4 °C. Subsequently, samples were filtered through a 0.2 μm cellulose acetate membrane syringe filter (VWR International, USA) to eliminate any protein aggregates or impurities. The WPI dispersions were then transferred into cylindrical screw-capped glass tubes (100 mm total length, 20 mm diameter) and subjected to thermal treatment at 80 °C

for 15 min, as per the previously optimized conditions. Following the thermal treatment, a specific volume of each Rb stock solution (previously dissolved in 0.1 mol L^{-1} Na_3PO_4), was introduced to the resultant WPI dispersions, followed by cooling in ice for 10 min to yield Rb-loaded WPI nanostructures. Additionally, the obtained nanostructures were submitted to a freezing process starting with −20 °C during 24 h in a regular freezer and followed by freezing until −80 °C in a laboratory grade freezer (Thermo Scientific, Massachusetts, USA). The freeze-drying experiment was conducted with a freeze-dryer (CHRIST – Alpha 1–4 LD plus, Germany), where solutions were placed for 2 days. After that period, the obtained nanostructures powders were stored at room temperature in a desiccator until further utilization.

2.2.2. Association efficiency of WPI nanostructures. To isolate free Rb in the supernatant, a solution containing 0.5 mL of Rb-loaded WPI nanostructures was introduced into Amicon® Ultra – 0.5 mL centrifugal filter units with a molecular weight cut-off of 3 kDa (Merck Millipore, Ireland). Subsequently, centrifugation (Model 5415 R, Eppendorf) at 16 000*g* was conducted for 20 min at 4 °C.[26] The spectrophotometric determination of unbound Rb in the filtrate occurred at 437 nm using a calibration curve ($y = 26.951x - 7 \times 10^{-5}$, $R^2 = 0.99$, where y and x represent absorbance and Rb concentration, respectively). These outcomes were employed to calculate the **association efficiency (AE)** using eqn (1). The concentrate containing Rb-loaded WPI nanostructures, retained in Amicon®, underwent drying at 55 °C for 24 h in a ventilated oven. The loading capacity (LC) was then determined by mass difference, following eqn (2).

$$\text{AE}\% = (\text{total Rb} - \text{free Rb})/\text{total Rb} \times 100 \quad (1)$$

$$\text{LC}\% = (\text{total Rb} - \text{free Rb})/\text{mass nanoparticles} \times 100 \quad (2)$$

2.3. Particle characterization

Size, polydispersity index (PdI), and surface charge (ζ-potential) of WPI nanostructures were evaluated through dynamic light scattering (DLS) with a Zetasizer Nano ZS (Malvern Instruments, United Kingdom), equipped with a He–Ne laser with a wavelength of 633 nm. This particle characterization method was applied to assess the effects of the freeze-drying process might have in the Rb-loaded WPI nanostructures in terms of size, PdI, and ζ-potential of WPI. All measurements were conducted at 25 °C in triplicate, with the results presented as the average ± standard deviation of the experimental values.

2.4. Cell viability assay

The cell viability assessment was conducted using the MTT conversion assay, following the methodologies outlined by Braz *et al.* (2017)[27] and Tibolla *et al.* (2019).[28] Caco-2 cells (passage number 20–35) in DMEM supplemented with 10% (v/v) FBS, 1% (v/v) PS and 1% (v/v) of NEAA solution were seeded at a density of 4×10^4 cells per well in a 96-well plate and incubated at 37 °C in a 5% CO^2 humidified atmosphere for 24 h. Briefly, various concentrations of WPI nanostructures, WPI nanostructures associated with Rb, and free Rb (ranging from 0.015 to 0.1 mg mL^{-1}) were diluted in supplemented DMEM medium and homogenized. Cells treated with DMEM alone served as the control. Subsequently, the DMEM medium was replaced with WPI samples, free Rb, and ethanol, maintaining the cells at 37 °C in a 5% CO_2 environment for an additional 24 h. After incubation, the samples were removed, and cells were washed with PBS. Following this, 100 μL of MTT solution (0.5 mg mL^{-1}) was added to each well, and the plate was incubated at 37 °C for 3 h to generate purple formazan crystals. The solubilization of these crystals involved adding 200 μL of DMSO to each well, followed by orbital shaking (100 rpm) for 30 min. The formazan was quantified by measuring the absorbance at 570 nm and 630 nm (used for background subtraction) in a Synergy™ HT Multi-mode Microplate Reader (Biotek Instruments, Winooski, VT, USA). Four replicates of each sample were analyzed. The percentage of cell viability for all samples was determined using eqn (3).

$$\text{Cell viability}\% = \text{Abs}_{\text{sample}}/\text{Abs}_{\text{control}} \times 100 \quad (3)$$

where $\text{Abs}_{\text{sample}}$ and $\text{Abs}_{\text{control}}$ are the absorbance of the cells + samples and the absorbance of cells (*i.e.*, cells in DMEM medium), respectively.

2.5. 3D food printing of carrot structures

2.5.1. Formulation of carrot inks. Carrot inks were prepared following the procedure previously optimized by Pant *et al.* (2021)[8] and Jeon *et al.* (2024),[17] with some modifications. Carrots were meticulously prepared by peeling, washing, and manual dicing. Subsequently, the diced carrots were cooked for 25 min in boiling water. After draining the water, the boiled carrots were carefully blended for 5 min until achieving a paste-like consistency, utilizing a handheld blender. To ensure smooth 3D printing without nozzle blockage, the resulting pastes were sieved in a stainless-steel sieve with 0.9 mm aperture size.

As presented in Table 1, increasing concentrations of XG, ranging from 0 to 1.2%, were added to the carrot pastes and mixed at 1500 rpm with a Hei-TORQUE overhead stirrer equipped with a propeller stirrer 3-blade from Heidolph instruments (Germany), in a water bath at 45 °C, for 20 min, to ensure an initial decline in XG viscosity and proper homogenization within the carrot paste. Prior to XG addition, WPI-Rb nanostructures were added to the carrot paste to ensure proper dispersion, reaching a final concentration of 5.2 mg mL^{-1}, following the previous mixing conditions, during 20 min. This concentration was based on the AE results that can be verified

Table 1 Representation of carrot ink formulations with different concentrations of XG and WPI-Rb nanostructures

	Ink 1	Ink 2	Ink 3	Ink 4	Ink 5
XG (%)	0	0.3	0.6	1.2	0.6
WPI-Rb nanostructures (%)	—	—	—	—	0.52

in section 3.1.1, and on Rb' daily recommended intake (*i.e.*, 1.3 mg day^{-1} for men and 1.1 mg day^{-1} for women).[29]

The obtained carrot inks, free from any particles that could obstruct the nozzle of the printer, were then stored in the refrigerator for future utilization.

The obtained carrot inks were dropped into a 10 mL Luer-lock syringe nozzle coupled with a micro tip (d = 1 mm). Carrot-filled syringes were placed into the print head of a Tissue Scribe 3D bioprinter from 3D Cultures (Philadelphia, USA) and further programmed.

2.5.2. 3D printing parameters. The widespread study of 3DPF in recent years stems from its advantageous applications in the food science and technology sector. This includes the ability to construct finished products with customized designs, shapes, flavors, nutritional profiles, textures, and consistencies through a streamlined process based on digital 3D models.[30,31] Within the realm of 3D printing technologies, this study uses extrusion-based 3DFP due to its simplicity and versatility in supporting various foods.[32–35] The CAD 3D design was performed using Fusion 360, Autodesk (California, USA). 3MF files of parallelepipeds (20 × 60 × 6 mm) were exported from the CAD software to import in the slicing software Ultimaker Cura 4.1.0 (Utrecht, The Netherlands). The line pattern of the projected carrot structures was printed at 20 mm s^{-1} with a layer height of 1 mm, layer width of 1 mm at the flow rate of 10% and infill density of 40%.

2.6. Carrot inks characterization

2.6.1. 3D printing' shape assessment and printability. The shape of 3D printed samples was assessed by visually comparison between the designed structure and the printed samples. The printability was evaluated by comparing the original dimensions of the CAD file with the dimensions of the extruded carrot ink filament (*i.e.*, width and height). The measurements were performed digitally, using the software ImageJ from National Institutes of Health (Maryland, United States).

2.6.2. Rheological analysis. The rheological properties of carrot inks were investigated utilizing an oscillatory rheometer (Discovery Hybrid Rheometer DHR-2, TA Instruments, Delaware, USA). Stainless steel parallel plates with a diameter of 40 mm and a truncation gap of 1000 μm were employed. To assess viscosity shear thinning, an up–down–up step program was performed at different shear rates ranging from 1 to 10001 s^{-1}. The shear thinning behavior was also characterized using the Herschel–Bulkley model – eqn (4).

$$\tau = \tau_0 + k\dot{\gamma}^n \quad (4)$$

where τ is the shear stress, τ_0 the yield stress, k the consistency index, $\dot{\gamma}$ the shear rate, and n the flow index.

Oscillation amplitude sweep tests were performed by applying a stress range from 0.1 to 2000 Pa at a constant frequency of 1 Hz to access the viscoelastic properties of the inks. All experiments were conducted at room temperature, in triplicate.

2.7. *In vitro* digestion of carrot inks incorporating nanostructures

WPI-Rb nanostructures, free Rb, carrot ink incorporating Rb, and carrot ink incorporating WPI-Rb nanostructures underwent an *in vitro* digestion process following the INFOGEST static *in vitro* digestion model adapted to the general older adult population.[36] This model simulates the oral, gastric, and intestinal phases of digestion of the elderly, where the rate of gastric emptying is slowed down from 2 to 3 h, the pH of the stomach content is higher (3.7), the amount of gastric and intestinal digestive enzymes and bile salts is lower. In the oral phase, 5 grams of the sample was combined with simulated salivary fluid (SSF) containing KCl, KH_2PO_4, $NaHCO_3$, $MgCl_2(H_2O)_6$, $(NH_4)_2CO_3$, HCl, and $CaCl_2(H_2O)_2$. α-Amylase (1875 IU mL^{-1}) was added due to the presence of starch in the carrot samples. The mixture underwent a 2 min incubation at 37 °C with orbital agitation at 120 rpm. Moving to the gastric phase, simulated gastric fluid (SGF) containing KCl, KH_2PO_4, $NaHCO_3$, NaCl, $MgCl_2(H_2O)_6$, $(NH_4)_2CO_3$, HCl, $CaCl_2(H_2O)_2$, and pepsin solution (1200 IU mL^{-1}) was added, adjusting the pH to 3.7. The mixture was incubated for 3 h under similar conditions. Subsequently, the intestinal phase comprised simulated intestinal fluid (SIF) containing KCl, KH_2PO_4, $NaHCO_3$, NaCl, $MgCl_2(H_2O)_6$, HCl, $CaCl_2(H_2O)_2$, bile salts (6.7 mmol L^{-1}), and pancreatin solution (800 IU mL^{-1}). The pH was adjusted to 7.0, and the samples were incubated for an additional 2 h. After the intestinal phase, the reaction was stopped by adding 1 mmol L^{-1} of enzyme inhibitor pefabloc® SC and samples were cooled in ice for 15 min until further collection.

2.8. Riboflavin's bioaccessibility

Rb's bioaccessibility was assessed utilizing a method adapted from Pinheiro *et al.* (2013).[37] 10 mL samples of digested carrot inks, nanostructures, and Rb underwent centrifugation (Allegra 64R, Beckman Coulter, USA) at 18 000*g* for 30 min at 25 °C. The resulting separation yielded two distinct phases: an opaque sediment phase at the bottom and a supernatant (micelle phase) at the top. The micelle phase, presumed to contain the bioactive compound (*i.e.*, the bioaccessible fraction), was considered available for absorption and metabolic processing.[38] Subsequently, 5 mL aliquots of the supernatant were collected to quantify the released bioactive compound post *in vitro* digestion. Rb concentration was determined through fluorescence spectroscopy using a microplate reader (BioTek™ Cytation™ 3, USA) with excitation at 450 nm and emission at 530 nm. Standard Rb solutions facilitated the creation of a calibration curve (y = 1 000 000x + 1006; R^2 = 0.97), where y represents fluorescence and x represents Rb concentration. Blank fluorescence subtraction corrected the fluorescence intensity. Rb bioaccessibility (eqn (5)) was determined as reported by Akça *et al.* (2019)[39] using eqn (4):

$$\text{Bioaccessibility } (\%) = C_{\text{Micelle Phase}}/C_{\text{Initial}} \times 100 \quad (5)$$

where $C_{\text{Micelle Phase}}$ is the concentration of Rb in the micelle phase, C_{Initial} is the concentration of Rb before *in vitro* digestion.

2.9. Statistical analysis

During this study, statistical analyses were performed to every data from each of the experimental results. Therefore, the mean values and standard deviations of the experimental data were calculated. Statistical analysis of the data was carried out using Analysis of Variance (ANOVA) and Tukey mean comparison test ($p < 0.05$), resorting to Origin® Pro 2018 software (Massachusetts, USA).

3. Results

3.1. Particles characterization

3.1.1. Association efficiency and loading capacity. WPI nanostructures demonstrated a notable ability to bind Rb with an AE of 59.2 ± 0.7% and a LC of 3.31 ± 0.43% at a concentration of 0.2 mg mL^{-1}. Above 0.05 mg mL^{-1}, the system retained the capability to associate with Rb, however, with a gradual decrease in efficiency. The system reached its maximum AE of 72.1 ± 2.6% at 0.05 mg mL^{-1}, however, as 0.2 mg mL^{-1} is 4 times more concentrated with a slight decrease in efficiency (12.9%), this was chosen as the optimal concentration for Rb association and further experiments; LC exhibited an increase with increasing Rb concentrations, indicating that WPI nanostructures can efficiently load Rb, reaching its maximum at 0.2 mg mL^{-1}. Other authors used β-lactoglobulin (main protein fraction of WPI) as encapsulant material and demonstrated similar results, where β-lactoglobulin nanostructures were able to encapsulate Rb at 0.105 mg mL^{-1} with an AE of 64.4 ± 0.9% and a LC of 1.80 ± 0.16%.[40] These findings confirm the selection of 0.2 mg mL^{-1} as the optimal Rb concentration for subsequent characterization and applications.

3.1.2. Particle size, polydispersity and zeta potential. During DLS measurements, an assessment of freeze-dried nanostructures was conducted concerning their size and PdI. This evaluation involved dissolving the powders of WPI-Rb nanostructures in aqueous media, as detailed in section 2.2.1. The obtained values for WPI-Rb dispersions were 65 ± 2.09 nm and 0.392 ± 0.49 for particle size and PdI, respectively. The storage stability at 4 °C and 25 °C (45 days) and a comparison between freeze-dried and liquid samples was assessed in terms of size and PdI (ESI, Fig. S1†). These findings align with and support the data reported in prior research studies.[25,41,42] Also, these experimental results provide structural information of Rb-loaded WPI nanostructures, under specific conditions, which validates their use in the following applications.

3.2. Cell viability

Cell viability is an essential parameter that needs careful assessment, particularly in the case of high bioactive compounds concentration and nanostructures, prior to any application, due to their nano size and large surface area per unit, which may increase the adherence and interaction with cell membranes. These phenomena may result in enhanced cellular uptake, leading to cellular damage and consequently, a decrease in the efficiency of bioactive compound absorption.[43] Therefore, the cell viability study was evaluated with WPI-Rb nanostructures, WPI nanostructures, and free Rb using Caco-2 cells with a 24-hour exposure period. In Fig. 1, it can be observed that, starting from a concentration of 0.050 mg mL^{-1} of free Rb, cellular viability decreases, reaching a low value (<10%) at 0.075 and 0.1 mg mL^{-1}. In contrast, we observed that the number of viable cells present after treatment with increasing concentrations of WPI nanostructures (up to 5 mg mL^{-1}) with and without Rb, after incubation for 24 h, was approximately 100%. This indicated that the nanostructures were non-toxic and reduce significantly free Rb negative effect to the cells at the dilution concentrations and exposure times tested. On one hand, prior investigations have reported the

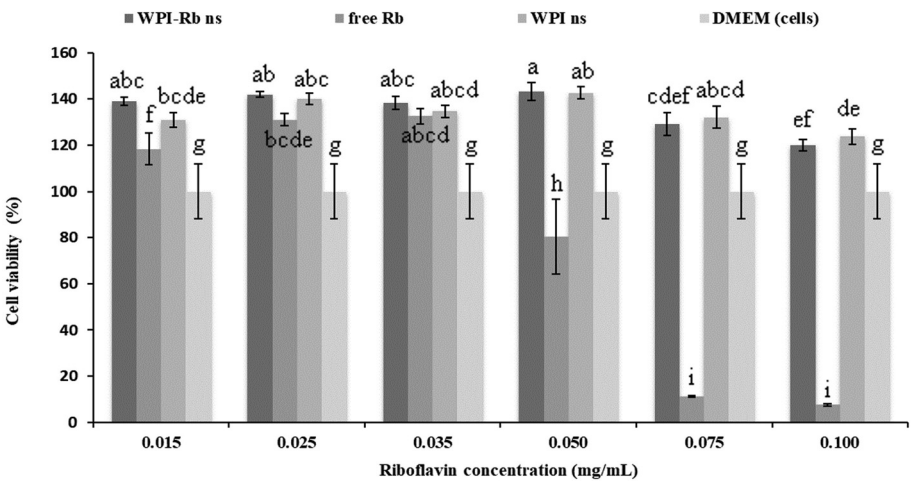

Fig. 1 Caco-2 cell viability following a 24 h incubation period in the presence of WPI nanostructures, WPI-Rb nanostructures, and free Rb. The bars in the graph depict the standard deviation. Statistical significance between samples is denoted by distinct lowercase superscripts (a–d) for each concentration ($p < 0.05$).

absence of cytotoxic effects on Caco-2 cells exposed to high internal phase Pickering emulsion encapsulating bioactive compounds, previously stabilized with WPI nanoparticles (up to 10 mg mL^{-1}).[44] On the other hand, Simões *et al.* (2020) have shown the adverse effect of β-lactoglobulin nanostructures with or without Rb on Caco-2 cells in a similar range of concentrations, comparing with WPI nanostructures.[45]

3.3. 3D printing of carrot inks

3.3.1. Printability and shape assessment. For this study, one model (*i.e.*, paralepidid) with a crossed lines infill was designed to allow the observation and measurement of the filament within the pattern. The size and format of this model was also designed to ease the 3D printing process and to obtain simple structures for further evaluation. Printability accuracy (*i.e.*, deviation from geometrical parameters), infill resolution and shape fidelity assessments imply visual evaluation and measurements of 3D printed samples to compare with the digitally designed ones. These methodologies are crucial to tune up the food formula and 3D printing parameters towards adequate extrudability, filament formation and shape retention. Following this line, the formulated inks (Table 1) with increasing concentrations of XG were added to the base carrot pastes in order to modify their rheological properties, which directly impacts their resolution, printability and shape. By visualizing the obtained 3D printed samples (Fig. 3A–D) it can be readily seen that the ink 1 presented the lowest infill resolution, shape fidelity and surface quality. Regarding ink 2 (Fig. 2B), the addition of 0.3% XG may have improved printability and shape fidelity; however, it presents poor resolution in the infill filaments, respective holes and structure walls. For inks 3 and 4, an improvement can be observed, particularly in the filament infill section, with no changes from one to another, thus, meaning that it is not necessary to add XG above 0.6% (ink 3) at its final concentration. However, the shape retention of the wall's filaments that can be observed from a top view in Fig. 3A–D is not satisfactory, giving the increased width and lack of homogeneity that was promoted by the ink flow during the printing process. These may be related not only to the food ink rheological characteristics, but also to determined 3D printing parameters such as printing speed, flow, number of walls, and travel movements, among others Heck *et al.* (2023) investigated the influence of the extrusion process on the stability of XG-starch based printed objects.[46] The authors reported similar results in terms of filament height and width' deviation from the projected geometrical parameters, respectively, and attributed this behavior to the slumping effect,[47] where the material flows in the transverse directions because of the hydrostatic pressure and to a correlation between printing speed and the ink's viscoelastic properties (*i.e.*, storage modulus, G'). Finally, the authors concluded that the stability of the inner and outer structure of 3DPF is highly dependent on their viscoelastic profile and specific 3D printing parameters.

Relatively good printability and shape retention were achieved in terms of the printed structure' area, meaning that the designed area is close to the printed and measured area of the parallelepiped carrot structures (as seen in Fig. 3A–D). One of the most important factors to evaluate the printability and resolution, is the difference between digitally designed filament and the printed ones. Visual differences can be seen by comparing the width of the extruded infill filament (Fig. 4B), which is 2.5 times wider than the designed ones (Fig. 4A). Also, although the height of the printed structures is nearly the same as the designed ones, there is a lack of definition in the 6 projected layers which can also be explained by the abovementioned slumping effect, reported by Heck *et al.* (2023).[46]

Regardless of the optimization that must be performed in terms of shape fidelity, resolution and printability, the visual inspection and the printability values obtained (Table 3) led to the provisional selection of ink 3 as the best formulation to study and incorporate the nanostructures. As expected, due to the physical properties of the nano structures, as reported in section 3.1.2 (*i.e.*, low size and polydispersity), in terms shape fidelity and resolution and printability, no relevant visual changes can be seen in ink 5, comparing to ink 3 and ink 4, (Fig. 2C, D and E). To confirm these outcomes and the selec-

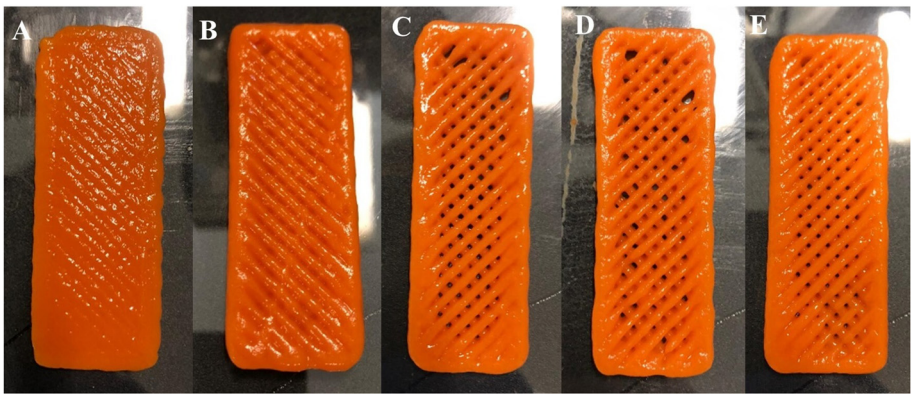

Fig. 2 Visual evaluation of 3D printed structures' shape with increasing xanthan gum concentration: (A) ink 1 – control, (B) ink 2 – 0.3%, (C) ink 3 – 0.6%, (D) ink 4 – 1.2% and (E) ink 5 – 0.6% + nanostructures.

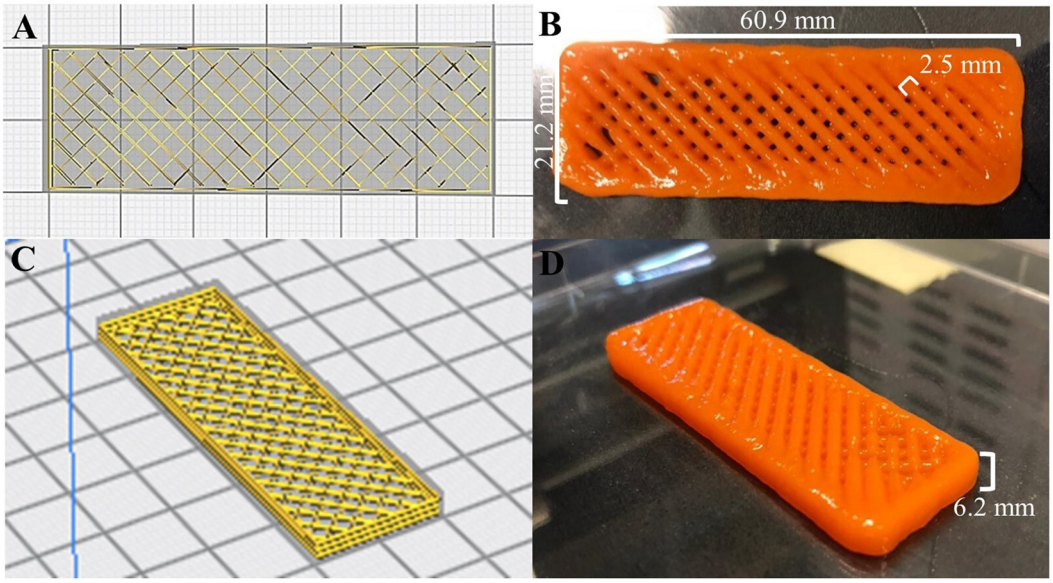

Fig. 3 3D-food structures in (A) and (C) digital, and (B) and (D) printed formats (ink 3). Bars and letters in the pictures indicate the digital measures of the 3D printed food structures.

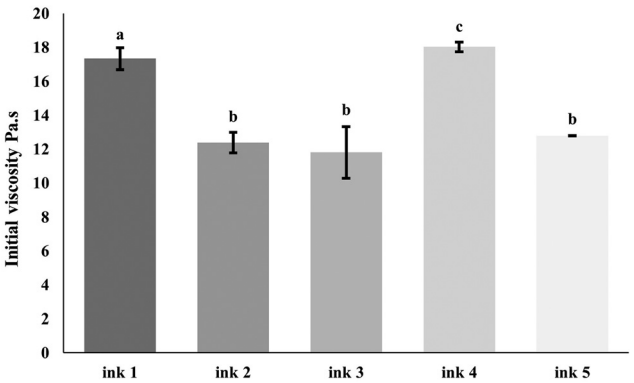

Fig. 4 Rheological characterization of carrot inks in terms of initial viscosity. The bars in the graph depict the standard deviation. Statistical significance (p < 0.05) between samples is denoted by distinct lowercase superscripts (a–d).

tion of the best formulation, a rheological characterization was performed.

3.3.2. Rheological characterization of 3D printed food structures. In the field of 3D extrusion-based methodologies, a food ink, initially in a quiescent bulk state, undergoes a transformative process. It experiences a shift to a high shear condition as it passes through the nozzle, adopting a new shape, ultimately attaining a renewed resting state.[48] This intricate interplay of rheological properties orchestrates the properties of foods during the 3D printing process, shaping their form and ensuring the success of the extrusion-based fabrication method. The crucial rheological characteristics governing these dynamic transitions of 3D printing encompass viscosity, viscoelastic behavior, elastic recovery, and shear stress. This study delves into a comprehensive characterization of inks modified with increasing XG concentrations, exploring their impact on rheology properties, shape, printability and infill resolution of 3D-printed carrot food inks. XG is a commonly used hydrocolloid with extensive application in the food industry due to its capacity to manipulate the rheological characteristics of food.[49,50] The five formulations of carrot inks consistently exhibited the desired shear-thinning pseudoplastic behavior, as the viscosity of these food inks exhibited an immediate decline with low shear rates (from 1 to 501 s^{-1}) (Table 2). Ultimately, when the shear rate started to decrease, the viscosity gradually increased, which contributes to preserve the shape of the printed structures. An unexpected phenomenon

Table 2 Representation of the yield stress (Pa), consistency index (k) and the flow index (n) as shear-thinning coefficients of the formulated inks

	Ink 1	Ink 2	Ink 3	Ink 4	Ink 5
Yield stress (Pa)	79.42	39.81	56.60	125.87	71.69
k	57.77	54.83	49.98	61.32	50.18
n	0.24	0.17	0.24	0.25	0.25
R^2	0.997	0.877	0.989	0.984	0.993

Table 3 Measurements of CAD and 3D-printed food structures and structure printability values

	CAD	Ink 1	Ink 2	Ink 3	Ink 4	Ink 5
Width (mm)	20	21.2	21.4	21.2	21.3	21.1
Length (mm)	60	61.5	61.3	60.9	61.0	59.9
Height (mm)	6	4.9	5.2	6.2	6.1	6.1
Printability	1	0.88	0.94	1.1	1.1	1.07

was identified in carrot ink 2 and 3, where the initial viscosity exhibited a substantial decrease upon the addition of XG in comparison to the control carrot ink 1 (as seen in Fig. 4). This observation aligns with findings from previous studies by Pant *et al.* (2021),[8] where a similar reduction in viscosity was reported after the incorporation of XG in carrot inks. The diminished viscosity is attributed to the influence of XG on other components within the food ink formulation such as carrot starch. Contrarily to this behavior, there is a point where a determined concentration of XG increases ink viscosity. This occurrence can be observed in ink 4 (Fig. 4), which contains XG at a concentration of 1.2%. Finally, by comparing ink 3 and 5, it can be concluded that the incorporation of WPI-Rb nanostructures did not affect the ink viscosity, probably due to the nano size of the structures and the low amount added to the ink (5.2 mg mL^{-1}).

Following the surpassing of yield stress for flow initiation, the continuous extrusion process is influenced by changes in viscosity with shear rate.[51] The shear rate dependency is assessed by fitting shear rate-viscosity profiles using the Herschel–Bulkley model (eqn (4)), enabling the analysis of consistency index (k) and flow index (n). In contrast to shear-thickening fluids ($n > 1$), shear-thinning fluids ($n < 1$) are generally preferred for printing applications. Table 2 shows that all inks exhibit non-Newtonian behavior, evident in a conspicuous decrease in viscosity with increasing shear rate (data not shown). The n values for all inks fall within the range of 0.17–0.25, which stands significantly below 1, indicating robust shear-thinning behavior.[52] Despite ink 2 theoretically demonstrating the most pronounced shear-thinning behavior (*i.e.*, lowest n value) among increasing XG concentrations, the results from infill resolution and shape assessment (section 3.3.1) revealed that ink 3 (*i.e.*, XG at 0.6%) exhibits superior accuracy in terms of shape fidelity and infill resolution. Ideally, low K and n values are advantageous for easing extrusion through the nozzle by reducing ink viscosity.[53] Considering these factors and reports, ink 3, with the lowest k value and a relatively low n value, provides an adequate extrusion. The incorporation of WPI-Rb nanostructures into ink 3 resulted in ink 5. As expected, comparing to ink 3, ink 5 showed no significant differences in terms of its initial viscosity, shear-thinning and viscoelastic behavior, although there was an increase on yield stress value, that can be attributed to the effect of WPI-Rb nanostructures powder on the food ink, that resulted in a slightly rigid matrix, which can be seen as an ideal indicator for better filament formation, as investigated elsewhere.[54]

In rheology, the loss modulus (G'') is the ratio of the viscous (out of phase) component to the stress and is related to the material's ability to dissipate stress through heat. The G' relates to the stored energy arising from the elastic deformation of materials and serves as a crucial metric, not only assessing extrudability but also gauging the shape retention of 3D printing materials during the deposition process.[48] The results from angular frequency sweep experiments revealed that G' for all inks consistently surpassed G'' values across the entire angular frequency spectrum. As a reflection of this result, the loss tangent or $\tan\delta$ (*i.e.*, ratio G''/G') was consistently below 1 (between 0.16 and 0.31), indicating that the viscoelastic nature of materials is predominantly solid-like behavior. In 3D printing, shape fidelity and elastic-like behaviors are often attributed to higher G' and lower $\tan\delta$ values.[55] However, a correlation with yield stress values must be performed to understand the desired balance between extrudability and shape retention.

The assessment of the linear viscoelastic region in a material involves conducting an oscillatory measurement at a constant frequency while gradually increasing stress or strain amplitude. Throughout this process, the measured moduli exhibit linearity until the critical strain threshold is surpassed. The termination of the linear region is marked by a reduction in viscosity or elastic modulus coupled with a rise in the phase shift.[55] All studied inks have shown viscoelastic behavior, although, with different G' and G'' magnitudes and inflection points along with increasing XG concentration. The G' and G'' exhibited relative stability until the inflection point, with G' surpassing G'', revealing that all inks presented a viscoelastic solid behavior ($G' > G''$). Jeon *et al.* (2024) investigated the effect of hydrocolloids incorporation in carrot/squid blends as edible inks for extrusion 3D printing. The authors obtained similar results in oscillatory measurements, and highlighted the inks supplemented with XG as capable of maintaining their elastic microstructure, resulting in the most printable inks.[17]

The correlation between yield stress and the extrusion performance in 3D printing is significant, as it represents the minimum pressure necessary to initiate fluid flow.[56] An increased yield stress imposes a demand for elevated pressure generated by the extrusion unit, facilitating the uninterrupted extrusion of inks throughout the 3D printing process. In this sense, opting for a lower yield stress is typically advantageous for seamless extrusion. In the context of food inks, the yield stress is specifically identified as the point of intersection between G' and G'' in a shear stress sweep test. Analyzing Table 2, it is evident that yield stress initially decreased as the XG concentration rises from ink 1 to ink 2. Subsequently, it exhibited an increase with a further elevation in XG from ink 2 to ink 4. Ultimately, these values experienced a reduction upon the introduction of WPI-Rb nanostructures into the selected ink formulation (*i.e.*, ink 5). Also, there are differences in effect on yield stress among hydrocolloids, which can be attributed to distinct physical and chemical interactions between the hydrocolloids and other food components, as well as variations in intermolecular mattings resulting from chain flexibility and conformational changes.[46] For example, Xing *et al.* (2022) demonstrated that the introduction of Arabic gum to a black fungus-based ink resulted in a reduction in yield stress. In contrast, in the present work, the addition of XG increased the yield stress, a phenomenon that can be attributed to distinct water mobilities, and molecular conformations induced by the interaction with these different hydrocolloids.[9]

3.4. Riboflavin bioaccessibility

The concept of bioaccessibility relates to the proportion of a bioactive compound liberated from its structure, presenting potential availability for absorption, as elucidated by previous research studies.[57,58] The observation of Rb bioaccessibility results (Fig. 5) unveils that 36.4 ± 0.9% of Rb in its free form, reaching the intestinal phase, holds for potential absorption. Fig. 5 highlights a slight increase (+5.8%, $p > 0.05$) in Rb bioaccessibility when associated with WPI nanostructures ($p < 0.05$). It is believed that the reduced size of WPI nanostructures enhances solubility and bioavailability, preventing undesired physical and chemical reactions while safeguarding bioactive compounds from degradation. When associated with WPI nanostructures and further incorporated into the carrot ink, Rb bioaccessibility was significantly increased (+23.1%, $p > 0.05$). This may suggest the occurrence of a synergistic effect between the carrot food matrix and WPI nanostructures, indicating that the absorption of a specific bioactive compound can be maximized through strategic association/encapsulation within a system coupled with an appropriate food matrix. In comparison with relevant scientific publications, the observed synergistic effect between the food matrix and nanostructures aligns with studies emphasizing the crucial role of nano-based delivery systems in enhancing bioavailability. Previous research often reports the incorporation of nanostructures encapsulating bioactive compounds in food matrices such as beverages, dairy, bakery, meat products and plant-based milk analogs with relative success regarding compounds bioactivity, shelf life, and sensory properties.[59] For example, Ubeyitogullari *et al.* (2019) studied the bioaccessibility of novel phytosterols nanoparticles in granola bars and puddings and reported enhanced bioaccessibility values in all digested food matrix.[60] This achievement was mainly attributed to the incorporation of phytosterols in nanoporous starch aerogels particles, and no synergistic effect was identified between the food matrices and nanoparticles. In this regard, there is a lack of research reporting the incorporation of nanostructures in 3DPF and moreover, the impact of foods on the bioaccessibility of nanoencapsulated bioactive compounds. Therefore, the present study arises as an opportunity to open this perspective of further research on the interactions between nano-based delivery systems and food matrices.

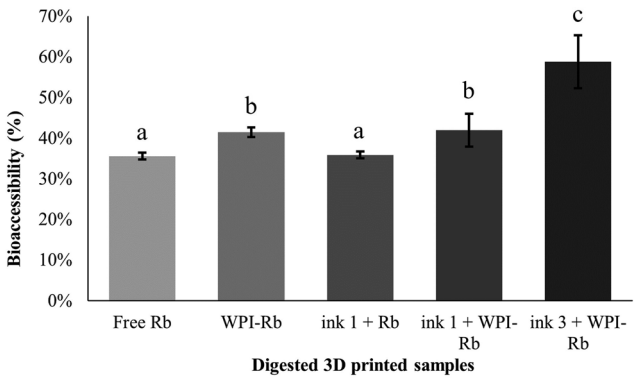

Fig. 5 Riboflavin bioaccessibility within carrot ink + WPI-Rb nanostructures, WPI-Rb nanostructures, free Rb, carrot ink + Rb (control). The bars in the graph depict the standard deviation. Statistical significance differences between samples are denoted by distinct lowercase superscripts (a–d).

4. Conclusions

This study underscores the promising potential of WPI nanostructures as an effective model of encapsulation of bioactive compounds. These nanostructures, characterized by a particle size of approximately 65 nm and a PDI of 0.392 have proven to be valuable candidates for associating Rb with an AE of approximately 60%. Notably, this association does not compromise the physical characteristics of the nanostructures. The biocompatibility assessment using Caco-2 cells revealed that their viability remained unaffected even at a concentration of 0.1 mg mL^{-1} of Rb in WPI nanostructures, demonstrating their safety for potential use in food applications. These results position Rb-loaded WPI nanostructures as promising fortifier agents in the food industry, providing a viable solution for enhancing nutritional content. Additionally, a carrot-based food matrix with adequate rheological characteristics for 3D printing has been formulated, in which the introduction of XG emerged as a pivotal factor, positively influencing the printability, structure, and shape of 3D printed carrot inks. This additive enhanced the overall quality of the printed food product. Lastly, the investigation into the 3D printed food matrix revealed a synergistic interaction with WPI nanostructures, particularly in terms of Rb bioaccessibility. This collaborative effect may enhance the overall bioavailability of Rb, highlighting the potential of these combined technologies (*i.e.*, nanotechnology and 3D food printing) for advancing food engineering and nutrition.

Author contributions

João Fernandes Araújo: writing – original draft, conceptualization, investigation, formal analysis, writing – review & editing; Jean-Michel Fernandes: writing – review & editing, investigation; Daniel Madalena: writing – review & editing and investigation; Raquel F.S. Gonçalves: writing – review & editing and investigation; Jorge M. Vieira: writing – review & editing, investigation and formal analysis; Joana T. Martins: writing – review & editing, investigation, formal analysis; António A. Vicente: writing – review & editing, supervision and funding acquisition; Ana C. Pinheiro: writing – review & editing, conceptualization, supervision, validation and funding acquisition.

Abbreviations

3DFP 3D food printing
3DPF 3D-printed foods

WPI	Whey protein isolate
Rb	Riboflavin
XG	Xanthan gum.

Data availability

The data supporting this article have been included as part of the ESI.†

Conflicts of interest

The authors declare that they have no known competing financial interests or personal relationships that could have appeared to influence the work reported in this paper.

Acknowledgements

João Fernandes Araújo, Jean-Michel Fernandes and Raquel F. Gonçalves acknowledge the Foundation for Science and Technology (FCT) for their fellowship (SFRH/BD/09849/2020, SFRH/BD/147286/2019 and SFRH/BD/140182/2018, respectively). Joana T. Martins and Ana C. Pinheiro acknowledge FCT for their Assistant Research contract obtained under the scope of Scientific Stimulus Employment with reference 2022.00788.CEECIND/CP1718/CT0024 and 2023.06513.CEECIND, respectively.

This work was supported by the Portuguese Foundation for Science and Technology (FCT) under the scope of the strategic funding of UIDB/04469/2020 unit, and by LABBELS – Associate Laboratory in Biotechnology, Bioengineering and Microelectromechanical Systems, LA/P/0029/2020.

References

1 B. Jagadiswaran, V. Alagarasan, P. Palanivelu, R. Theagarajan, J. A. Moses and C. Anandharamakrishnan, Valorization of food industry waste and by-products using 3D printing: A study on the development of value-added functional cookies, *Future Foods*, 2021, **4**, 100036.

2 A. Jędrusek-Golińska, D. Górecka, M. Buchowski, K. Wieczorowska-Tobis, A. Gramza-Michałowska and K. Szymandera-Buszka, Recent progress in the use of functional foods for older adults: A narrative review, *Compr. Rev. Food Sci. Food Saf.*, 2020, **19**, 835–856.

3 E. S. Yearick, M. S. L. Wang and S. J. Pisias, Nutritional status of the elderly: Dietary and biochemical findings, *J. Gerontol.*, 1980, **35**, 663–671.

4 R. K. Chandra, A. Imbach, C. Moore, D. Skelton and D. Woolcott, Nutrition of the elderly, *Can. Med. Assoc. J.*, 1991, **145**, 1475–1487.

5 L. Kourkouta, P. Ouzounakis, A. Monios and Ch. Iliadis, Nutritional habits in the elderly, *Prog. Health Sci.*, 2016, **6**(2), 155–159.

6 M. L. Wahlqvist, G. S. Savige and W. Lukito, Nutritional disorders in the elderly, *Med. J. Aust.*, 1995, **163**, 376–381.

7 A. Derossi, R. Caporizzi, D. Azzollini and C. Severini, Application of 3D printing for customized food. A case on the development of a fruit-based snack for children, *J. Food Eng.*, 2018, **220**, 65–75.

8 A. Pant, A. Y. Lee, R. Karyappa, C. P. Lee, J. An, M. Hashimoto, U. X. Tan, G. Wong, C. K. Chua and Y. Zhang, 3D food printing of fresh vegetables using food hydrocolloids for dysphagic patients, *Food Hydrocolloids*, 2021, **114**, 106546.

9 X. Xing, B. Chitrakar, S. Hati, S. Xie, H. Li, C. Li, Z. Liu and H. Mo, Development of black fungus-based 3D printed foods as dysphagia diet: Effect of gums incorporation, *Food Hydrocolloids*, 2022, **123**, 107173.

10 Y. Huang, M. Zhang and P. Pattarapon, Reducing freeze-thaw drip loss of mixed vegetable gel by 3D printing porosity, *Innovative Food Sci. Emerging Technol.*, 2022, **75**, 102893.

11 Y. O. Kewuyemi, H. Kesa and O. A. Adebo, Trends in functional food development with three-dimensional (3D) food printing technology: prospects for value-added traditionally processed food products, *Crit. Rev. Food Sci. Nutr.*, 2022, **62**, 7866–7904.

12 Y. J. Lin, P. Punpongsanon, X. Wen, D. Iwai, K. Sato, M. Obrist and S. Mueller, FoodFab: Creating Food Perception Illusions Using Food 3D Printing, in *Conference on Human Factors in Computing Systems - Proceedings*, Association for Computing Machinery, 2020.

13 R. Wu, J. Jiang, F. An, X. Ma and J. Wu, Research progress of 3D printing technology in functional food, powering the future of food, *Trends Food Sci. Technol.*, 2024, **149**, 104545.

14 F. Silva, T. Pereira, S. Mendes, L. Gordo and M. M. Gil, Consumer's perceptions and motivations on the consumption of fortified foods and 3D food printing, *Future Foods*, 2024, **10**, 100423.

15 I. Tomašević, P. Putnik, F. Valjak, B. Pavlić, B. Šojić, A. Bebek Markovinović and D. Bursać Kovačević, 3D printing as novel tool for fruit-based functional food production, *Curr. Opin. Food Sci.*, 2021, **41**, 138–145.

16 J. Ringquist, T. Phillips, B. Renner, R. Sides, K. Stuart, M. Baum and J. Flannery, Capitalizing on the shifting consumer food value equation, in *Capitalizing on the shifting consumer food value equation*, 2016.

17 E. Y. Jeon, Y. G. Chun and B.-K. Kim, Investigation of carrot/squid blends as edible inks for extrusion 3D printing: Effect of hydrocolloids incorporation, *J. Food Eng.*, 2024, **364**, 111777.

18 O. L. Ramos, R. N. Pereira, L. S. Simões, D. A. Madalena, R. M. Rodrigues, J. A. Teixeira and A. A. Vicente, Nanostructures of whey proteins for encapsulation of food ingredients, in *Biopolymer Nanostructures for Food Encapsulation Purposes*, 2019, vol. 1, pp. 69–100.

19 V. Amenta, K. Aschberger, M. Arena, H. Bouwmeester, F. Botelho Moniz, P. Brandhoff, S. Gottardo, H. J. P. Marvin, A. Mech, L. Quiros Pesudo, H. Rauscher, R. Schoonjans, M. V. Vettori, S. Weigel and R. J. Peters,

Regulatory aspects of nanotechnology in the agri/feed/food sector in EU and non-EU countries, *Regul. Toxicol. Pharmacol.*, 2015, **73**, 463–476.

20 A. Abbasi, Z. Emam-Djomeh, M. A. E. Mousavi and D. Davoodi, Stability of vitamin D3 encapsulated in nanoparticles of whey protein isolate, *Food Chem.*, 2014, **143**, 379–383.

21 O. L. Ramos, R. N. Pereira, R. Rodrigues, J. A. Teixeira, A. A. Vicente and F. Xavier Malcata, Physical effects upon whey protein aggregation for nano-coating production, *Food Res. Int.*, 2014, **66**, 344–355.

22 O. L. Ramos, R. N. Pereira, A. Martins, R. Rodrigues, C. Fuciños, J. A. Teixeira, L. Pastrana, F. X. Malcata and A. A. Vicente, Design of whey protein nanostructures for incorporation and release of nutraceutical compounds in food, *Crit. Rev. Food Sci. Nutr.*, 2017, **57**, 1377–1393.

23 J. Yi, L. Gao, G. Zhong and Y. Fan, Fabrication of high internal phase Pickering emulsions with calcium-cross-linked whey protein nanoparticles for β-carotene stabilization and delivery, *Food Funct.*, 2020, **11**, 768–778.

24 O. L. Ramos, R. N. Pereira, R. M. Rodrigues, J. A. Teixeira, A. A. Vicente and F. X. Malcata, Whey and Whey Powders: Production and Uses, in *Encyclopedia of Food and Health*, 1st edn, 2015, vol. 5, pp. 498–505.

25 L. S. Simões, J. F. Araújo, A. A. Vicente and O. L. Ramos, Design of β-lactoglobulin micro- and nanostructures by controlling gelation through physical variables, *Food Hydrocolloids*, 2020, **100**, 105357.

26 M. A. Azevedo, A. I. Bourbon, A. A. Vicente and M. A. Cerqueira, Alginate/chitosan nanoparticles for encapsulation and controlled release of vitamin B2, *Int. J. Biol. Macromol.*, 2014, **71**, 141–146.

27 L. Braz, A. Grenha, D. Ferreira, A. M. Rosa da Costa, C. Gamazo and B. Sarmento, Chitosan/sulfated locust bean gum nanoparticles: In vitro and in vivo evaluation towards an application in oral immunization, *Int. J. Biol. Macromol.*, 2017, **96**, 786–797.

28 H. Tibolla, F. M. Pelissari, J. T. Martins, E. M. Lanzoni, A. A. Vicente, F. C. Menegalli and R. L. Cunha, Banana starch nanocomposite with cellulose nanofibers isolated from banana peel by enzymatic treatment: In vitro cytotoxicity assessment, *Carbohydr. Polym.*, 2019, **207**, 169–179.

29 D. Turck, J.-L. Bresson, B. Burlingame, T. Dean, S. Fairweather-, M. Heinonen, K.-I. Hirsch-Ernst, I. Mangelsdorf, H. J. McArdle, A. Naska, G. Nowicka, K. Pentieva, Y. Sanz, A. Siani, M. Stern, D. Tomé, H. Van Loveren, M. Vinceti, P. Willatts, H. Przyrembel, I. Tetens, C. Dumas, L. Fabiani, C. Forss, S. Ioannidou and M. Neuhäuser-Berthold, Dietary Reference Values for riboflavin, *EFSA J.*, 2017, **15**(8), 4919.

30 J. M. Habibur, N. Islam, K. Ahmed, A. Khosla, M. Kawakami and H. Furukawa, Heliyon Rheological and mechanical properties of edible gel materials for 3D food printing technology, *Heliyon*, 2020, **6**, e05859.

31 L. Masbernat, S. Berland, C. Leverrier, G. Moulin, C. Michon and G. Almeida, Structuring wheat dough using a thermomechanical process, from liquid food to 3D-printable food material, *J. Food Eng.*, 2021, **310**, 110696.

32 T. Carranza, P. Guerrero, K. de la Caba and A. Etxabide, Texture-modified soy protein foods: 3D printing design and red cabbage effect, *Food Hydrocolloids*, 2023, **145**, 109141.

33 S. B. Kokane, P. R. Anjaly, S. Thangalakshmi and V. K. Arora, Current trends in additive manufacturing based 4D food printing technology: A review, *Future Foods*, 2024, **10**, 100450.

34 J. Sun, W. Zhou, L. Yan, D. Huang and L. ya Lin, Extrusion-based food printing for digitalized food design and nutrition control, *J. Food Eng.*, 2018, **220**, 1–11.

35 S. J. Rowat, R. L. Legge and C. Moresoli, Plant protein in material extrusion 3D printing: Formation, plasticization, prospects, and challenges, *J. Food Eng.*, 2021, **308**, 110623.

36 O. Menard, U. Lesmes, C. S. Shani-Levi, A. Araiza Calahorra, A. Lavoisier, M. Morzel, A. Rieder, G. Feron, S. Nebbia, L. Mashiah, A. Andres, G. Bornhorst, F. Carrière, L. Egger, S. Gwala, A. Heredia, B. Kirkhus, A. Macierzanka, R. Portman, I. Recio, V. Santé-Lhoutellier, C. Tournier, A. Sarkar, A. Brodkorb, A. Mackie and D. Dupont, Static in vitro digestion model adapted to the general older adult population: an INFOGEST international consensus, *Food Funct.*, 2023, **14**, 4569–4582.

37 A. C. Pinheiro, M. Lad, H. D. Silva, M. A. Coimbra, M. Boland and A. A. Vicente, Unravelling the behaviour of curcumin nanoemulsions during in vitro digestion: effect of the surface charge, *Soft Matter*, 2013, **9**, 3147–3154.

38 H. D. Silva, E. Beldíková, J. Poejo, L. Abrunhosa, A. T. Serra, C. M. M. Duarte, T. Brányik, M. A. Cerqueira, A. C. Pinheiro and A. A. Vicente, Evaluating the effect of chitosan layer on bioaccessibility and cellular uptake of curcumin nanoemulsions, *J. Food Eng.*, 2019, **243**, 89–100.

39 S. N. Akça, H. S. Sargın, Ö. F. Mızrak and M. Yaman, Determination and assessment of the bioaccessibility of vitamins B1, B2, and B3 in commercially available cereal-based baby foods, *Microchem. J.*, 2019, **150**, 104192.

40 L. S. Simões, L. Abrunhosa, A. A. Vicente and O. L. Ramos, Suitability of β-lactoglobulin micro- and nanostructures for loading and release of bioactive compounds, *Food Hydrocolloids*, 2020, **101**, 105492.

41 D. A. Madalena, Ó. L. Ramos, R. N. Pereira, A. I. Bourbon, A. C. Pinheiro, F. X. Malcata, J. A. Teixeira and A. A. Vicente, In vitro digestion and stability assessment of β-lactoglobulin/riboflavin nanostructures, *Food Hydrocolloids*, 2016, **58**, 89–97.

42 S. Rikhtehgaran, I. Katouzian, S. M. Jafari, H. Kiani, L. A. Maiorova and H. Takbirgou, Casein-based nanodelivery of olive leaf phenolics: Preparation, characterization and release study, *Food Struct.*, 2021, **30**, 100227.

43 H.-K. Ha, J. W. Kim, M.-R. Lee, W. Jun and W.-J. Lee, Cellular Uptake and Cytotoxicity of β-Lactoglobulin Nanoparticles: The Effects of Particle Size and Surface Charge, *Asian-Australas. J. Anim. Sci.*, 2015, **28**, 420–427.

44 J. Yi, L. Gao, G. Zhong and Y. Fan, Fabrication of high internal phase Pickering emulsions with calcium-cross-

linked whey protein nanoparticles for β-carotene stabilization and delivery, *Food Funct.*, 2020, **11**, 768–778.

45 L. S. Simões, J. T. Martins, A. C. Pinheiro, A. A. Vicente and O. L. Ramos, β-lactoglobulin micro- and nanostructures as bioactive compounds vehicle: In vitro studies, *Food Res. Int.*, 2020, **131**, 108979.

46 M. P. Heckl, M. Korber, M. Jekle and T. Becker, Relation between deformation and relaxation of hydrocolloids-starch based bio-inks and 3D printing accuracy, *Food Hydrocolloids*, 2023, **137**, 108326.

47 A. R. Fahmy, T. Becker and M. Jekle, 3D printing and additive manufacturing of cereal-based materials: Quality analysis of starch-based systems using a camera-based morphological approach, *Innovative Food Sci. Emerging Technol.*, 2020, **63**, 102384.

48 S. Zhu, M. A. Stieger, A. J. van der Goot and M. A. I. Schutyser, Extrusion-based 3D printing of food pastes: Correlating rheological properties with printing behaviour, *Innovative Food Sci. Emerging Technol.*, 2019, **58**, 102214.

49 H. M. Cho and B. Yoo, Rheological Characteristics of Cold Thickened Beverages Containing Xanthan Gum–Based Food Thickeners Used for Dysphagia Diets, *J. Acad. Nutr. Diet.*, 2015, **115**, 106–111.

50 W. Jo, J. H. Bak and B. Yoo, Rheological characterizations of concentrated binary gum mixtures with xanthan gum and galactomannans, *Int. J. Biol. Macromol.*, 2018, **114**, 263–269.

51 A. Dick, B. Bhandari, X. Dong and S. Prakash, Food Hydrocolloids Feasibility study of hydrocolloid incorporated 3D printed pork as dysphagia food, *Food Hydrocolloids*, 2020, **107**, 105940.

52 N. Paxton, W. Smolan, T. Böck, F. Melchels, J. Groll and T. Jungst, Proposal to assess printability of bioinks for extrusion-based bioprinting and evaluation of rheological properties governing bioprintability, *Biofabrication*, 2017, **9**, 044107.

53 Y. Cheng, Y. Fu, L. Ma, P. L. Yap, D. Losic, H. Wang and Y. Zhang, Rheology of edible food inks from 2D/3D/4D printing, and its role in future 5D/6D printing, *Food Hydrocolloids*, 2022, **132**, 107855.

54 A. Schwab, R. Levato, M. D'Este, S. Piluso, D. Eglin and J. Malda, Printability and Shape Fidelity of Bioinks in 3D Bioprinting, *J. Am. Chem. Soc.*, 2020, **120**, 11028–11055.

55 J. M. Vieira, F. D. Oliveira, D. B. Salvaro, G. P. Maffezzolli, J. D. B. de Mello, A. A. Vicente and R. L. Cunha, Rheology and soft tribology of thickened dispersions aiming the development of oropharyngeal dysphagia-oriented products, *Curr. Res. Food Sci.*, 2020, **3**, 19–29.

56 Y. Liu, X. Liang, A. Saeed, W. Lan and W. Qin, Properties of 3D printed dough and optimization of printing parameters, *Innovative Food Sci. Emerging Technol.*, 2019, **54**, 9–18.

57 R. F. S. Gonçalves, J. T. Martins, C. M. M. Duarte, A. A. Vicente and A. C. Pinheiro, Advances in nutraceutical delivery systems: From formulation design for bioavailability enhancement to efficacy and safety evaluation, *Trends Food Sci. Technol.*, 2018, **78**, 270–291.

58 B. Demir, M. Gürbüz, J. Çatak, H. Uğur, E. Duman, Y. Beceren and M. Yaman, In vitro bioaccessibility of vitamins B1, B2, and B3 from various vegetables, *Food Chem.*, 2023, **398**, 133944.

59 R. F. S. Gonçalves, D. A. Madalena, J. M. Fernandes, M. Marques, A. A. Vicente and A. C. Pinheiro, Application of nanostructured delivery systems in food: From incorporation to detection and characterization, *Trends Food Sci. Technol.*, 2022, **129**, 111–125.

60 A. Ubeyitogullari and O. N. Ciftci, In vitro bioaccessibility of novel low-crystallinity phytosterol nanoparticles in non-fat and regular-fat foods, *Food Res. Int.*, 2019, **123**, 27–35.